ADVANCED FUNCTIONAL MATERIALS
www.afm-journal.de

Coordinated Multi-Component Gradient Engineering of Catalyst Layers for Advanced Polymer Electrolyte Fuel Cells

Shangwei Zhou, Matt P. Tudball, Yiming Guo, Bia Brandt, Adam Zucconi, Wenjia Du, Junfu Bu, Daniel H. C. Wan, Jianuo Chen, Emanuele Magliocca, Feng Ryan Wang, Alexander J.E. Rettie, Patrick S. Grant, Paul R. Shearing, Rhodri Jervis, and Thomas S. Miller**

Membrane electrode assemblies (MEAs) are critical to emerging energy technologies such as polymer electrolyte fuel cells (PEFCs), but their performance is often limited by challenges in reactant transport, ionic conduction and water management within the catalyst layer (CL). Conventional CL architectures, whether uniform or layered, struggle to manage these competing transport phenomena effectively, leading to mass transport losses, poor proton conduction and structural inconsistencies. To address these limitations, this study presents a continuous linear gradient CL design that breaks from traditional approaches. By employing a precision-controlled dual-nozzle spray coating technique, a smooth gradient in Pt/C ratio, ionomer content and ionomer type is fabricated across the CL thickness. Uniquely, this method relies exclusively on commercially available materials, strategically positioned where they are most effective. The resulting architecture aligns with natural electrochemical gradients in the CL, facilitating improved reactant accessibility, proton transport and water handling. This structure not only enhances performance under realistic operating conditions but also improves long-term durability. Furthermore, by selectively placing materials only where needed, it has the potential to reduce overall material usage and cost. This gradient approach offers a scalable and practical path toward next-generation, high-efficiency PEFCs.

1. Introduction

Membrane electrode assemblies (MEAs) lie at the heart of many electrochemical technologies that require efficient ion and electron transport, including electrolysers, redox flow batteries and fuel cells. Among these, polymer electrolyte fuel cells (PEFCs) have emerged as one of the leading candidates for clean energy applications due to their high efficiency, compact design and zero-emission operation.[1–4] Despite their potential, the widespread deployment of PEFCs is still constrained by the high cost of materials and performance limitations, challenges that are particularly concerning for the catalyst layer (CL), which governs key electrochemical processes. Conventional CLs for PEFCs feature a homogeneous distribution of Pt and ionomer throughout the layer, producing the triple phase boundary (TPB), where the catalyst, electrolyte and reactant gas meet [5,6] to enable electrochemical reactions such as the

S. Zhou, M. P. Tudball, Y. Guo, B. Brandt, A. Zucconi, D. H. C. Wan, J. Chen, E. Magliocca, A. J. E. Rettie, R. Jervis, T. S. Miller
Electrochemical Innovation Lab
Department of Chemical Engineering
University College London
London WC1E 7JE, UK
E-mail: shangwei.zhou.20@ucl.ac.uk; t.miller@ucl.ac.uk

S. Zhou, M. P. Tudball, Y. Guo, A. J. E. Rettie, R. Jervis, T. S. Miller
Advanced Propulsion Lab
Department of Chemical Engineering
University College London
London WC1E 6BT, UK

The ORCID identification number(s) for the author(s) of this article can be found under https://doi.org/10.1002/adfm.202518360

B. Brandt
Process Systems Engineering (AVT.SVT)
RWTH Aachen University
Forckenbeckstraße 51, 52074 Aachen, Germany

A. Zucconi
HORIBA UK
Kyoto Close, Moulton Park, Northampton NN3 6FL, UK

W. Du, P. R. Shearing
Department of Engineering Science
University of Oxford
Parks Road, Oxford OX1 3PJ, UK

W. Du, P. R. Shearing
Oxford Martin School
University of Oxford
Oxford OX1 3BD, UK

W. Du, P. R. Shearing
The ZERO Institute
University of Oxford
Oxford OX2 0ES, UK

DOI: 10.1002/adfm.202518360

oxygen reduction reaction (ORR). Unfortunately, homogeneously constructed PEFCs suffer from heterogeneity in the distribution of current, pressure, reactant concentration, water distribution and temperature, leading to numerous unintended gradients across the fuel cell, which drive non-uniform catalyst utilisation and accelerate degradation of the catalyst, support and other components.[7,8] This "intrinsic heterogeneity" within traditional PEFCs has a significant negative impact on both cell performance and lifetime.[9]

Recent studies have demonstrated that introducing gradients in CL components can enhance performance while reducing material usage. Gradient engineering has been considered via two strategies: "across the layer" from the membrane/CL interface to the gas diffusion layer (GDL).[10] and "in the catalyst plane" from the gas inlet to the outlet, to counteract the depletion of reactants.[11] For example, when the catalyst loading is graded along the reactant flow direction,[12–15] it offers improvements in both cell performance and uniformity in the distributions observed. In-plane gradient strategies focus on addressing reactant depletion, optimising the composition across the CL and balancing proton- and mass-transport. Elsewhere, ionomer optimisation studies have focused on determining the optimal ionomer-to-carbon ratio,[16–18] often assuming a uniform distribution from the membrane/CL interface to the GDL. Ionomer films directly influence proton conduction from the membrane and impact pore structure formation, which affects reactant access to Pt sites; however, insufficient ionomer near the membrane increases proton transport resistance, while excessive ionomer near the GDL hinders gas-phase flow. To address these challenges, a gradient in ionomer distribution, with higher ionomer concentration near the membrane and lower concentration near the GDL.[19–21] has been used to enhance performance by improving proton conduction while minimising mass transport losses.

Beyond efficient ion transport, the ORR also requires efficient electron transport through the Pt/C network from the GDL. Therefore, combined catalyst-ionomer gradient designs have also been investigated. Venkatesh et al.[12] and Shen et al.[22] advocated for higher Pt loading near the membrane. Increasing Pt loading near the membrane while reducing it near the GDL minimises transport resistance, increases reaction rates, and improves Pt utilisation. Elsewhere, a novel approach by Huang et al.[23] introduced a multi-ionomer gradient design using both long-side-chain (LSC) and short-side-chain (SSC) ionomers. They found that incorporating SSC ionomers near the membrane improved proton conductivity, while LSC ionomers near the GDL enhanced mass transport. This approach improved water management, reduced ohmic resistance, and increased overall fuel cell performance.

Despite growing interest in gradient-engineered CLs for enhancing fuel cell performance, current designs remain constrained by fundamental limitations. Most rely on discrete, multi-layer architectures, typically two or a few layers at most, with abrupt transitions between materials. These configurations may introduce additional interfaces and can act as centres for degradation, as well as additional interfacial resistances and mechanical instabilities. Sequential spray-coating is commonly used to build multiple layers by stacking distinct catalyst slurries. However, this process complicates manufacturing by introducing adhesion issues, interlayer defects and high sensitivity to deposition conditions. More advanced designs, such as five-layer CLs,[24] attempt to mitigate these abrupt transitions through incremental layering, leading to modest performance and durability gains. Again, they fall short of delivering a seamless gradient and increase process complexity, making scalability difficult. Previously, continuous linear gradient structures, those with truly smooth compositional transitions across the CL thickness, were only achievable in simulations.[25–27] Experimental realisation of such gradients remained elusive due to limitations in material control and processing methods.

In this work, physical barriers introduced by multi-layer step-by-step gradients have been overcome by innovating a high-precision spray-coating technique to fabricate a truly smooth gradient CL structure, marking a fundamental difference from conventional, discontinuous multi-layer designs. This method enables the practical realisation of continuous compositional gradients, which were previously only achievable by theoretical or simulation. The design integrates controlled gradients in Pt loading (wt.%), ionomer-to-carbon (I/C) ratio and ionomer chemistry, offering a refined approach to CL architecture. The electrochemical performance of these gradient CLs has been thoroughly evaluated under a range of operating conditions and benchmarked against non-gradient counterparts using accelerated stress tests to assess long-term durability. In addition, X-ray computed tomography (CT) scans of both pristine and aged MEAs are conducted to quantitatively assess structural degradation in the CL. The results demonstrate the potential of this approach to advance high-performance, cost-effective PEFCs for commercial deployment. While the methodology is showcased here in fuel cells, it is broadly applicable to other electrochemical devices, such as electrolysers and CO_2 reduction systems, where interfacial optimisation and efficient catalyst utilisation are critical. By enabling a more continuous and uniform catalyst morphology, this strategy overcomes key limitations of traditional CLs, including poor mass transport, interfacial resistance, and uneven electrochemical activity distribution. The full workflow covering fabrication, characterisation and MEA testing is outlined in Figure S1 (Supporting Information) for clarity and reproducibility.

2. Methodology

2.1. Ink Preparation, Spray Coating and Activation

Two catalyst inks were prepared with different ionomer and catalyst formulations. The first ink (ink1) contained 60% platinum

W. Du, J. Bu, P. S. Grant, P. R. Shearing, R. Jervis, T. S. Miller
The Faraday Institution, Quad One
Harwell Science and Innovation Campus
Didcot OX11 ORA, UK

J. Bu, P. S. Grant
Department of Materials
University of Oxford
Oxford, United Kingdom

D. H. C. Wan, F. R. Wang
Materials and Catalysis Laboratory
Department of Chemical Engineering
University College London
London WC1E7JE, UK

supported on high-surface-area Ketjenblack EC-300J (Fuel Cell Store), with a crystallite size of 2–3 nm, and Aquivion D72-25BS ionomer (Total Acid Capacity: 1.35–1.43 meq g^{-1}), with I/C ratios of 0.9, 0.85, and 0.8. The second ink (ink2) used 40% platinum on the same carbon support, with a smaller crystallite size of 1.5–2.5 nm, and Nafion D2020CS ionomer (Total Acid Capacity: 1.03–1.12 meq g^{-1}), with I/C ratios of 0.7, 0.65, and 0.6. Additionally, reference samples without a gradient were prepared using 40% Pt/C with Aquivion ionomer and a constant I/C ratio of 0.75. To ensure uniform dispersion, a solvent mixture of deionised water (18.2 mΩ resistivity) and isopropanol (6:4 by weight) was used. The ink preparation followed a controlled sequence: catalyst first, then water, followed by isopropanol, and finally ionomer to prevent burst fires. The solid content was maintained at 5 mg mL^{-1} to prevent nozzle clogging during spray coating. The ink was initially homogenised using a vortex mixer (RX3, Velp Scientifica) for 30 s, then ultrasonicated (VWR USC900TH) in an ice bath for 30 min to achieve a stable dispersion.

A 6 cm × 3 cm, 250 µm-thick Freudenberg H23C6 carbon paper with a microporous layer (MPL) was placed on a heated plate of a Sono-Tek spray coater equipped with dual nozzles. Positioned at a 25° angle, the nozzles ensured uniform coating distribution. The heated plate was maintained at 80 °C to facilitate rapid solvent evaporation. For mixed-based CLs, the catalyst ink was sprayed at a constant flow rate of 0.1 mL min^{-1} per nozzle. In contrast, the gradient spray-coating process involved multiple spray passes, with nozzle 1 gradually increasing its flow rate from 0 to 0.2 mL min^{-1} while nozzle 2 simultaneously decreased from 0.2 to 0 mL min^{-1}. The flow rates could be adjusted based on the desired gradient direction. The shaping air pressure remained at 1 bar throughout the process. The carbon paper was secured under an acrylic gasket with a 2.6 cm × 5.2 cm cutout to define the coating area. Pt loading was determined by weighing the substrate before and after the spray-coating process using a high-precision microbalance (Sartorius MCA66S-3S00-D), with the mass difference corresponding to the deposited catalyst.

2.2. MEA Hot Compression and Fuel Cell Testing

The MEA was fabricated by sandwiching a Gore Select membrane (GORE M735.18, USA) between the spray-coated gas diffusion electrode (GDE) as the cathode and a commercial GDE (HyPLAT, South Africa) as the anode. The commercial GDE featured a Pt loading of 0.4 mg cm^{-2} and was based on Freudenberg H23C9 carbon paper with a 15 µm MPL subjected to hydrophobic treatment. The MEA was hot-pressed between steel plates using a Carver hot press (USA) at 150 °C for 3 min under 1000 psi of compression (with four MEAs processed per batch). To prevent mechanical damage and displacement, Kapton film sheets were placed between the MEA and the steel plates.

Fuel cell testing was conducted using a custom-designed single PEFC with a 5 cm^2 active area. To ensure uniform compression, 18 mm-thick stainless-steel endplates were used, with a PTFE sheet placed between the endplate and the gold-coated current collector for electrical insulation. The 2 mm thick graphite flow-field plates featured a two-channel serpentine design with channel and rib dimensions of ≈1.14 mm in width and 1 mm in depth. DBK Enclosures heaters (100–240 V AC, 60 W) were affixed to both sides of the endplates to ensure uniform heating, preventing local hotspots and vapour condensation. Gas tightness and proper MEA compression were maintained using three layers of 0.076 mm PTFE gaskets on both sides of the MEA, while 12 bolts around the endplates provided uniform compression.

For the performance evaluation, the fuel cell was operated at 60/80 °C using a commercial Scribner 850e test bench for precise temperature and humidification control. Hydrogen and air were supplied at a flow rate of 0.5 and 1.2 L min^{-1}, respectively, without applied back pressure. High-purity gases, including nitrogen (99.9%), air (99.9%), and hydrogen (99.995%), were used to maintain consistent operating conditions.

2.3. CL/MEA Characterisation

A Thermo Scientific Helios G4 PFIB CXe DualBeam Plasma Focused Ion Beam/Scanning Electron Microscope (FIB-SEM), equipped with an Oxford Instruments Ultim Max 170 Energy Dispersive X-ray (EDS) detector, was used for cross-sectional SEM imaging and EDS analysis. The process involved initial milling with a high ion beam current to rapidly remove material and create a trench, followed by stepwise polishing with lower currents to achieve a smooth surface. For cross-sectional SEM preparation, a high ion beam current (up to 2.5 µA) at 30 keV was first applied to efficiently mill the material and form a trench around the region of interest. After trench formation, the ion beam current was gradually reduced for fine polishing, with a final polishing step performed at 15 nA before SEM imaging and EDS mapping. This approach enhanced surface smoothness and minimised damaged layers, ensuring high-quality imaging and analysis. For SEM imaging, 2, 5 or 10 kV and 0.1 nA were used to capture detailed images of the sample's surface structure, while 10 kV and 1.6 nA were used for EDS mapping.

X-ray CT was conducted using a ZEISS Versa 620 instrument with a tungsten target. A 3 mm diameter disc was cut from each sample for imaging to allow for a balance between X-ray attenuation (signal-to-noise) and the representative volume. The imaging was conducted using a source voltage of 80 kV; a combination of geometrical and optically coupled magnification was deployed using a 4X magnification objective lens, binning of 1, an exposure time of 6 s, and 2001 projections. These parameters gave a voxel size of 0.73 µm and a field of view (FOV) of ≈1.5 mm. The tomograms were reconstructed using XMReconstructor software. The processing and analysis of the datasets were conducted using Avizo software (Thermo Scientific). The thickness measurements were made using an area of 0.25 mm^2, which is expected to be representative of the larger whole MEA.[28]

2.4. Fuel Cell Durability Test

The fuel cell durability test was conducted by following the accelerated degradation test (ADT) protocol suggested by the US Department of Energy (DOE).[29] In brief, the MEA was tested under a constant flow of H_2-N_2 with a square wave potential cycling between 0.6 and 0.95 V with 3s hold at each potential for 30k cycles. For every 10k cycles, fuel cell performance was evaluated by cyclic voltammetry and polarisation curve measurements. A

voltage recovery step was applied before every performance measurement.

3. Results and Discussion

3.1. Gradient Engineering and Fuel Cell Performance

On the cathode side of a PEFC, oxygen concentration is highest near the gas diffusion GDL and decreases as it diffuses into the CL, due to the consumption of oxygen at the TPB during the electrochemical reaction. Similarly, proton concentration within the CL decreases from the catalyst-membrane interface toward the interior of the CL, as protons are consumed. This creates concentration gradients for both oxygen and protons across the CL.[30,31] To optimise the cathode CL structure for improved proton conductivity, oxygen diffusion and water management, a dual-nozzle spraying system (as shown in **Figure** 1A) was employed to fabricate a smooth, controlled gradient in the CL (Figure 1B,C, see methods). This technique enables precise and dynamic control over the I/C ratio (Figure 1D), ionomer type (Figure 1E) and Pt weight percentage (Figure 1F), ensuring a continuous gradient across the CL. This design features a high ionomer fraction near the membrane to enhance proton transport, reduce ohmic losses and improve adhesion. A lower Pt/C ratio near the GDL facilitates oxygen diffusion and optimises mass transport.

To better address the interdependent factors and investigate the comprehensive effect of gradient engineering on fuel cell performance, two distinct catalyst inks were employed for the dual-nozzle system, each tailored for specific functional regions within the CL. Nozzle 1 sprayed an ink with a higher ionomer-to-carbon (I/C) ratio, higher platinum (Pt) weight percentage and short-side-chain (SSC) ionomer, which is applied near the membrane interface. In contrast, Nozzle 2 sprayed an ink with a lower I/C ratio, lower Pt weight percentage and long-side-chain (LSC) ionomer, which is applied near the GDL. The tested configurations included: (i) Baseline: A uniform CL with a constant I/C ratio of 0.75, 40 wt.% Pt/C and SSC ionomer. (ii) Mixed: A uniform CL prepared by blending ink1 (I/C 0.85, 60 wt.% Pt/C, SSC) and ink2 (I/C 0.65, 60 wt.% Pt/C, LSC), resulting in an average I/C of 0.75. (iii) Mink1_Gink2: A continuous gradient transitioning from ink1 near the membrane to ink2 near the GDL. (iv) Mink2_Gink1: A continuous gradient transitioning from ink2 near the membrane to ink1 near the GDL. (v) Two-layer: A conventional bilayer CL with ink1 adjacent to the membrane and ink2 adjacent to the GDL.

FIB-SEM was used to analyse CL morphology and elemental distribution, as shown in **Figure** 2A., focused Ga^+ ion beam was utilised to create a cross-section for subsequent EDS mapping (Figure 2A), and the corresponding elemental maps of F, S, and Pt.[32] are presented in Figure 2D–F.

By integrating the elemental signals along the X direction and the Y direction (from the membrane to the GDL, where the membrane side is at the top and the MPL/GDL is at the bottom, distinct trends in elemental distribution were observed. Along the Y direction, the Mink1_Gink2 sample exhibited higher intensities of ionomer (F and S signals) and Pt content near the membrane side, with a gradual decrease toward the GDL side, confirming the effectiveness of the smooth gradient engineering approach. Conversely, along the X direction, the F, S, and Pt elements were evenly distributed, indicating uniform composition within the plane of the CL. Additionally, SEM imaging of the Mink1_Gink2 and constant 0.75 I/C CLs is shown in Figure 2B,C. The images reveal that the Mink1_Gink2 CL exhibits a less porous structure on the CL surface, with a calculated surface porosity of 19.0% (measured using ImageJ), compared to 23.6% for the constant 0.75 I/C CL, as higher ionomer contents may form a denser ionomer network.[33] This difference is likely due to the higher I/C ratio (0.85 I/C) used near the membrane side, which leads to a denser microstructure, potentially enhancing proton transport.

The performance of fuel cells incorporating both uniform and gradient-engineered CLs was systematically evaluated under conditions without backpressure, as shown in Figure 2G,H. The I/C ratio is optimised from experiments, as shown in Figure S6 (Supporting Information), and the Pt loading is ≈0.25 mg cm^{-2}. Following the activation procedure, the baseline fuel cell with a uniform 0.75 I/C CL exhibited a peak power density of 725.71 mW cm^{-2} (Figure 2J), a limiting current density of 2008.8 mA cm^{-2} (Figure 2K), and an ECSA of 37.00 m^2 g^{-1}(calculated based on Figure 2L). The mixed CL, which replaced half of the catalyst and ionomer with 60% Pt/C and an LSC ionomer, resulted in a slight performance increase, reaching 769.15 mW cm^{-2} and 2066.5 mA cm^{-2}, along with a modest increase in ECSA to 38.38 m^2 g^{-1}. However, when the same materials were strategically optimised through gradient engineering, the Mink1_Gink2 configuration demonstrated a substantial performance enhancement, achieving a peak power density of 881.77 mW cm^{-2} and a limiting current density of 2269 mA cm^{-2}, representing increases of 156.06 mW cm^{-2} and 260.2 mA cm^{-2} compared to the baseline. Notably, this performance also surpassed any individual optimisation previously discussed, such as a single I/C gradient or independent variations in Pt wt.% and ionomer type, while also achieving the highest ECSA of 40.40 m^2 g^{-1}. Notably, our results were achieved under less favourable conditions, ambient pressure and air, compared to the DOE's rated power status of 890 mW cm^{-2}, which was obtained under 150 kPa back pressure. This highlights the effectiveness of our gradient-engineered CL design. Furthermore, the repeatability of our findings was confirmed by testing three different gradient configurations (shown in Figure S6, Supporting Information), consistently showing superior performance compared to the uniformly mixed counterpart in all cases.

This improvement can be attributed to the precise spatial distribution of materials within the CL. In the membrane-proximal region, the CL is optimised for proton transport by incorporating the SSC ionomer, which has a higher density of sulfonic acid groups, thereby enhancing proton conductivity. The increased Pt loading ensures maximum catalytic activity, particularly crucial in the high-proton flux region. Additionally, the higher I/C ratio promotes water retention, mitigating dehydration under high-current conditions. Conversely, in the GDL-proximal region, the CL is designed to enhance oxygen diffusion and mitigate flooding by incorporating the LSC ionomer, which exhibits lower water uptake and greater hydrophobicity. The reduced Pt loading in this region lowers material costs while maintaining sufficient catalytic activity for the ORR. Furthermore, the lower I/C ratio introduces larger interparticle

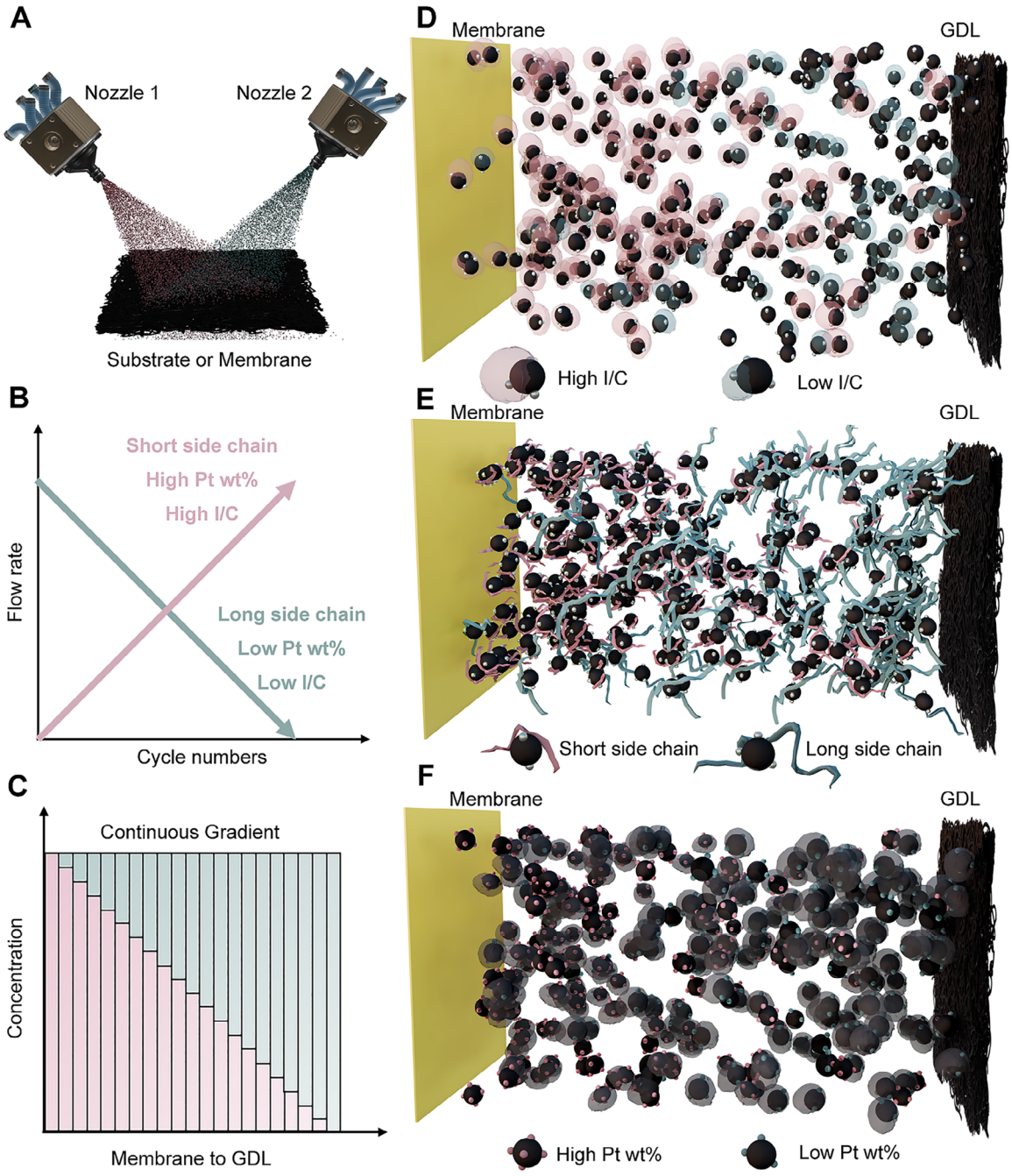

Figure 1. A) Schematic of the two-spray nozzle setup. B) Schematic of the nozzle flow rate to achieve a continuous, smooth gradient. C) Schematic of the continuous gradient. D) Schematic of the continuous gradient of the I/C ratio, transitioning from higher near the membrane to lower near the GDL. E) Schematic of the transition from short-side-chain ionomer near the membrane to long-side-chain ionomer near the GDL. F) Schematic of the continuous gradient of the Pt weight percentage (wt.%), transitioning from higher near the membrane to lower near the GDL.

pores, improving gas permeability and overall mass transport efficiency.

In contrast, the Mink2_Gink1 configuration resulted in the poorest performance, with a peak power density of 616.56 mW cm^{-2} and a limiting current density of 1708.8 mA cm^{-2}, along with the lowest ECSA of 31.66 m^2 g^{-1}. This decline in performance aligns with expectations, as the misplacement of materials disrupts optimal transport properties within the CL. EIS measurements at 1000 mA cm^{-2}, shown in Figure 2I, further support these findings. The Mink1_Gink2 CL exhibited the lowest Ohmic resistance, charge transfer resistance and mass transport resistance, confirming its superior performance.[34] Additionally, pre-activation fuel cell performance trends mirrored post-activation results, indicating that the observed

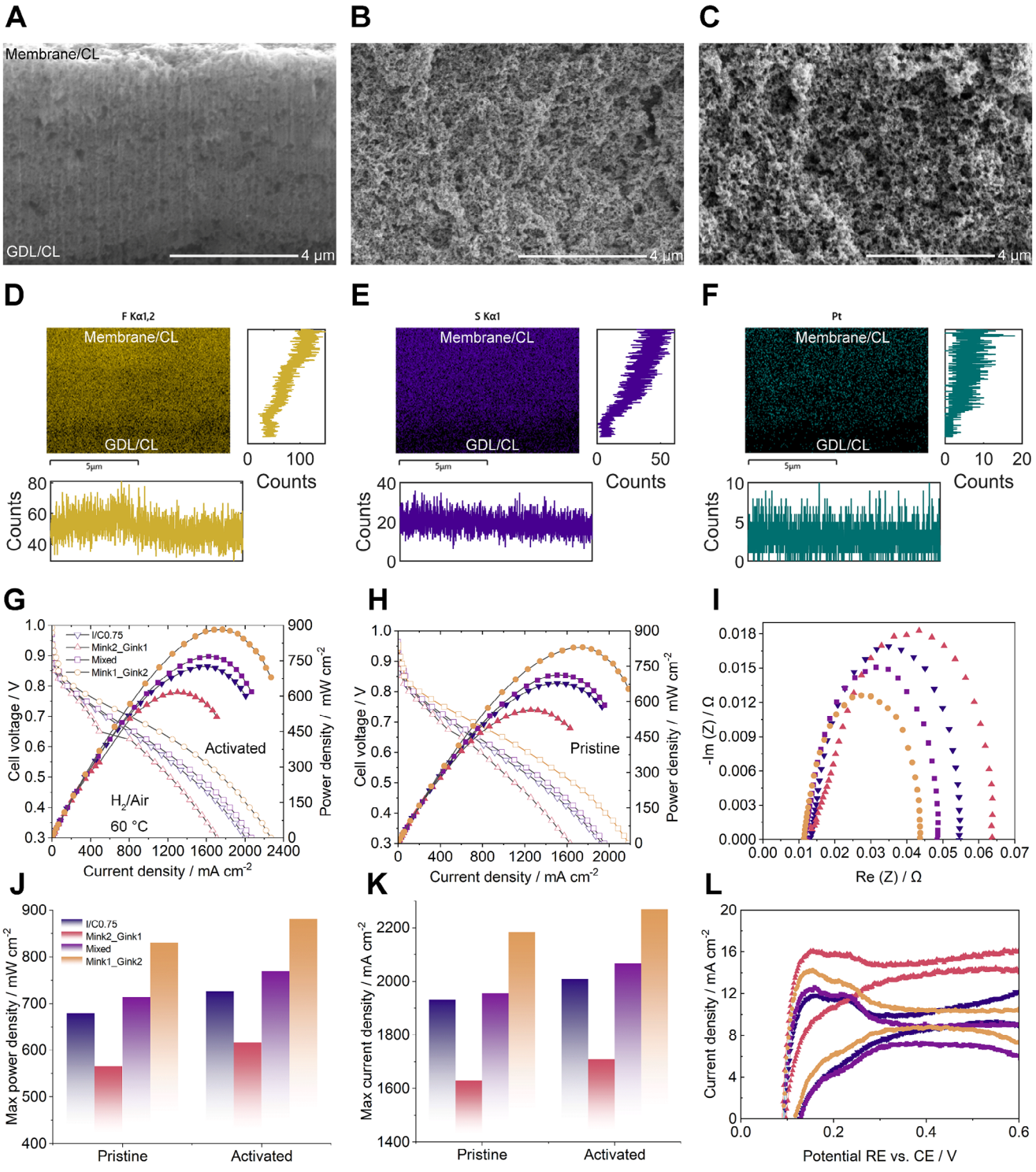

Figure 2. A) FIB cross-section of the Mink1_Gink2 CL prepared for EDS analysis. B) SEM image of the Mink1_Gink2 CL. (C) SEM image of the constant 0.75 I/C CL. D–F) Elemental distribution of fluorine (F), Sulfur (S), and platinum (Pt) obtained from 2D EDS mapping, with integrated elemental intensities along the X direction (perpendicular to Y) and Y direction (from membrane to GDL). (G-H) Polarisation and power density curves of the cells using the baseline, mixed, Mink1_Gink2, and Mink2_Gink1- CL under activated G) and pristine H) conditions. I) EIS measurements at 1000 mA cm^{-2}. J,K) Peak power density (J) and maximum current density (K, at 0.3 V) under activated and pristine conditions. L) Cyclic voltammetry curves for the cell using the baseline, mixed, Mink1_Gink2, and Mink2_Gink1- CL.

improvements were intrinsic to the gradient engineering strategy rather than an artefact of the activation process. By dynamically adjusting the flow rates of the two nozzles during the spraying process, a smooth and continuous gradient across the CL was imposed by gradual alteration of ink ratios, optimising proton conductivity, oxygen diffusion, and water management. These results highlight gradient-engineered CLs as a powerful strategy for enhancing fuel cell performance, surpassing the capabilities of uniformly mixed CLs. The effects of heterogeneously distributing each individual component were explored (Note S1, Supporting Information).

3.2. Durability Testing

Accelerated stress testing (AST) was conducted to evaluate the long-term durability of the Mink1_Gink2 gradient-engineered CL compared to both a 0.75 constant I/C and a two-layer CL, which served as controls (**Figure 3**). As previously discussed, conventional gradient strategies often suffer from interlayer defects caused by abrupt transitions in material composition. This issue is clearly observed in the two-layer CL, where the interface between the layers is easily recognisable (Figure S7A,D–F, Supporting Information). In contrast, the continuous gradient structure in our design avoids these sharp boundaries, improving mechanical integrity and potentially enhancing durability.

At the initial state, the gradient-engineered CL exhibited a peak power density of 1045.9 mW cm^{-2} and a limiting current density of 2826.1 mA cm^{-2} (Figure 3A), outperforming both the 0.75 constant I/C CL (951.36 mW cm^{-2} and 2600.9 mA cm^{-2}, Figure 3D) and the two-layer CL (825.96 mW cm^{-2} and 2359.4 mA cm^{-2}, Figure S7B, Supporting Information). Notably, this initial performance meets or surpasses previously reported values under similar temperature conditions but with 50–100 kPa of applied backpressure,[35–39] underscoring the effectiveness of the smooth gradient catalyst architecture under practical, zero-backpressure conditions. The lower performance of the two-layer CL is attributed to the fact that the two ink formulations were designed to form a coordinated multicomponent gradient during spray-coating, and neither was individually optimised for a standalone layered structure.

During the initial 10k cycles, all three CL configurations experienced notable performance degradation. The gradient-engineered CL exhibited reductions of 249.27 mW cm^{-2} in peak power density and 641.2 mA cm^{-2} in limiting current density. The 0.75 constant I/C CL showed decreases of 201.11 mW cm^{-2} and 511.2 mA cm^{-2}, while the two-layer CL dropped by 181.04 mW cm^{-2} and 472.4 mA cm^{-2}. This early-stage degradation is primarily associated with severe mechanical and chemical stresses affecting the ionomer and catalyst. Loss of sulfonic acid groups.[40] reduces proton conductivity and weakens ionomer–catalyst adhesion, while catalyst dissolution and agglomeration.[41] result in decreased ECSA (Figure 3B,E; Figure S7C, Supporting Information). Despite these effects, the gradient-engineered CL maintained superior performance to both controls throughout the first 10k cycles. These results indicate that while gradient architecture improves initial durability, long-term stability remains strongly governed by intrinsic material degradation mechanisms[42] motivating further ionomer and catalyst optimisation for PEFCs.

After 20k cycles, the peak power densities of the gradient-engineered and constant I/C CLs declined to 705.63 and 679.07 mW cm^{-2}, respectively, while the two-layer CL dropped to 587.35 mW cm^{-2} (Figure 3C,F). At EOT, the gradient-engineered and constant I/C CLs further declined to 645.2 and 626.52 mW cm^{-2}, whereas the two-layer CL fell to 551.0 mW cm^{-2}. Regarding limiting current density, the constant I/C CL slightly exceeded the gradient-engineered CL at EOT (1811.4 vs 1775.6 mA cm^{-2}), although both remained higher than the two-layer CL. Overall, from initial testing through EOT, the gradient-engineered CL consistently demonstrated enhanced performance retention relative to the non-gradient CLs, confirming that a continuous ionomer–catalyst gradient effectively minimises interfacial instability and supports long-term cell operation.

X-ray CT was used to quantify the degradation of the cathode CL before and after the AST. Different components within the MEA were distinguishable based on their pixel values (Figure 3G), allowing for accurate separation (see methods). Thickness was calculated by dividing the segmented volume of the cathode-side CL by its projected area, giving an average value. The thickness of the gradient-engineered CL decreased from 11.90 to 10.42 µm (Figure 3H,I), retaining 87.56% of its original thickness after 40k cycles. For the sample with a constant 0.75 I/C ratio, the thickness decreased from 12.45 to 11.29 µm (Figure 3J,K), corresponding to 90.68% of the original thickness. The similar degradation behaviour observed in both cases indicates that the smooth gradient design does not introduce additional defects, such as delamination, compared to the uniform CL. Additionally, the CL with a constant 0.75 I/C ratio exhibited a rougher surface, which is consistent with the SEM results.

Beyond the smooth linear gradient demonstrated in this study, more complex gradient architectures can be realised by dynamically modulating the nozzle flow rates in non-linear patterns (Figure S8A–C, Supporting Information). This approach enables precise spatial control over CL composition, paving the way for future investigations into advanced gradient designs (Figure S8D–I, Supporting Information) tailored to specific performance or durability needs.

4. Conclusion

This study presents an innovative continuous linear gradient CLs design, developed using a precise dual-nozzle spray coating technique. Unlike traditional uniform or discrete multi-layered CLs, this approach enables a smooth, controlled gradient transition in the Pt/C ratio, ionomer content, and ionomer type, optimising proton conduction, oxygen diffusion and mass transport simultaneously. Beyond the linear gradient, dynamic adjustment of the nozzle flow rate allows for the creation of various gradients in the future. Quantitative analysis demonstrates the superior performance of this smooth gradient CL structure. The optimal gradient design, featuring a higher ionomer-to-carbon (I/C) ratio, increased Pt weight percentage and SSC ionomer near the membrane side, achieved a peak power density of 881.77 mW cm^{-2} and a limiting current density of 2269 mA cm^{-2} at 60 °C with back pressure applied. In comparison, the

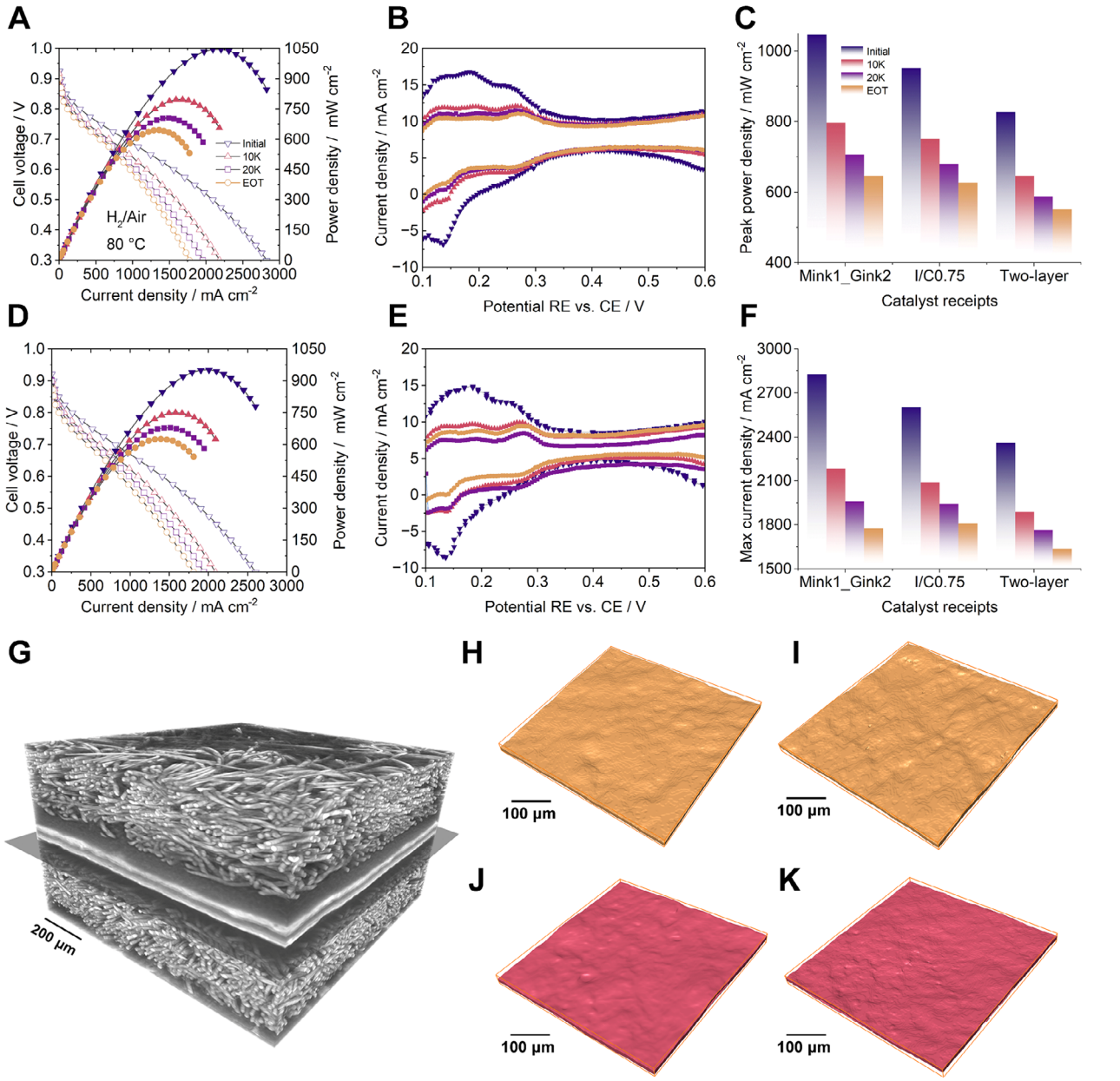

Figure 3. A,B) Polarisation and power density curves (A) and cyclic voltammetry curves (B) of the Mink1_Gink2 gradient-engineered CL from the initial state to the EOT. C) Comparison of peak power density for the Mink1_Gink2 gradient-engineered CL, the 0.75 constant I/C CL, and the two-layer CL from the initial state to EOT. D,E) Polarisation and power density curves (D) and cyclic voltammetry curves (E) of the 0.75 constant I/C CL from the initial state to the EOT. F) Comparison of maximum current density for the Mink1_Gink2 gradient-engineered CL, the 0.75 constant I/C CL, and the two-layer CL from the initial state to EOT. G) 3D volume rendering of the MEA. H,I) Segmented images of the Mink1_Gink2 gradient-engineered CL on the cathode side in the fresh state (H) and after AST (I), with the membrane-facing side up. J,K) Segmented images of the 0.75 constant I/C CL on the cathode side in the fresh state (J) and after AST (K), with the membrane-facing side up.

baseline CL with a constant I/C ratio of 0.75 exhibited a lower peak power density of 725.71 mW cm^{-2} and a limiting current density of 2008.8 mA cm^{-2}.

Under accelerated stress testing, the gradient-engineered CL demonstrated superior initial performance and maintained a performance edge throughout long-term cycling. Although both the gradient, conventional two-layer and uniform CLs experienced early degradation due to chemical and mechanical stresses affecting the ionomer and catalyst, the gradient design sustained higher power outputs over time. Structural analyses using CT and SEM confirmed that the gradient architecture did not introduce additional mechanical instability, such as delamination, despite some reduction in layer thickness. Overall, the continuous gradient CL approach offers a scalable, high-performance alternative to traditional designs, paving the way for next-generation fuel cell technology with enhanced efficiency and longevity.

Supporting Information

Supporting Information is available from the Wiley Online Library or from the author.

Acknowledgements

This work was carried out with funding from the UK Engineering and Physical Sciences Research Council (EPSRC) – EP/W03395X/1, EP/X023656/1, EP/W033321/1. PRS was supported by the Department of Science, Innovation and Technology (DSIT) and the Royal Academy of Engineering under the Chair in Emerging Technologies programme. WD and PRS acknowledge Oxford Martin School funding. JB and PSG acknowledge the use of characterisation facilities within the David Cockayne Centre for Electron Microscopy at the Department of Materials, University of Oxford.

Conflict of Interest

The authors declare no conflict of interest.

Data Availability Statement

The data that support the findings of this study are available from the corresponding author upon reasonable request.

Keywords

Advanced manufacturing, graded electrode, gradient, PEMFC, proton exchange membrane fuel cell, spray printing

Received: July 16, 2025
Revised: November 2, 2025
Published online:

[1] T. A. Suter, K. Smith, J. Hack, L. Rasha, Z. Rana, G. M. A. Angel, P. R. Shearing, T. S. Miller, D. J. L. Brett, *Adv. Energy Mater.* **2021**, *11*, 2101025.
[2] K. Smith, F. Foglia, A. J. Clancy, D. J. Brett, T. S. Miller, *Adv. Funct. Mater.* **2023**, *33*, 2304061.
[3] J. Chen, X. Lu, L. Wang, W. Du, H. Guo, M. Rimmer, H. Zhai, Y. Liu, P. R. Shearing, S. J. Haigh, S. M. Holmes, T. S. Miller, *Nat. Commun.* **2024**, *15*, 10811.
[4] S. Zhou, R. Jervis, *Chem. Methods* **2024**, *4*, 202300030.
[5] M. Wang, J. Zhang, S. Favero, L. J. R. Higgins, H. Luo, I. E. L. Stephens, M.-M. Titirici, *Nat. Commun.* **2024**, *15*, 9390.
[6] F. Zhang, B. Zu, B. Wang, Z. Qin, J. Yao, Z. Wang, L. Fan, K. Jiao, *Joule* **2025**, *9*, 101853.
[7] L. Cheng, K. Khedekar, M. Rezaei Talarposhti, A. Perego, M. Metzger, S. Kuppan, S. Stewart, P. Atanassov, N. Tamura, N. Craig, I. V. Zenyuk, C. M. Johnston, *Adv. Energy Mater.* **2020**, *10*, 2000623.
[8] K. Khedekar, M. Rezaei Talarposhti, M. M. Besli, S. Kuppan, A. Perego, Y. Chen, M. Metzger, S. Stewart, P. Atanassov, N. Tamura, N. Craig, L. Cheng, C. M. Johnston, I. V. Zenyuk, *Adv. Energy Mater.* **2021**, *11*, 2101794.
[9] S. Zhou, L. Rasha, L. Xu, W. Du, P. R. Shearing, M.-O. Coppens, D. J. L. Brett, R. Jervis, *Energy Convers. Manage.* **2023**, *297*, 117717.
[10] Y. Xu, G. Chang, R. Fan, T. Cai, *Chem. Eng. J.* **2023**, *451*, 138924.
[11] Y. Wang, L. Qi, F. Ma, H. Li, S. Ma, C. Wang, W. He, S. Wang, *Appl. Energy* **2025**, *378*, 124874.
[12] V. B. KP, G. Varghese, T. V. Joseph, P. Chippar, *Int. J. Hydrogen Energy* **2022**, *47*, 4018.
[13] M. Santis, S. A. Freunberger, A. Reiner, F. Büchi, *Electrochim. Acta* **2006**, *51*, 5383.
[14] D. P. Wilkinson, J. St-Pierre, *J. Power Sources* **2003**, *113*, 101.
[15] L. Yang, K. Fu, X. Jin, S. Wang, Q. Gan, Q. Zhang, P. Li, C. Cao, *Chem. Eng. Sci.* **2022**, *263*, 118132.
[16] S. M. Jayawickrama, D. Wu, R. Nakayama, S. Ishikawa, X. Liu, G. Inoue, T. Fujigaya, *J. Power Sources* **2021**, *496*, 229855.
[17] X. Lyu, T. Van Cleve, E. Young, J. Li, H. Yu, D. A. Cullen, K. C. Neyerlin, A. Serov, *J. Power Sources* **2023**, *556*, 232530.
[18] H. Ishikawa, Y. Sugawara, G. Inoue, M. Kawase, *J. Power Sources* **2018**, *374*, 196.
[19] S. Shahgaldi, A. Ozden, X. Li, F. Hamdullahpur, *Energy Convers. Manage.* **2018**, *171*, 1476.
[20] K. KIM, H. KIM, K. LEE, J. JANG, S. LEE, E. CHO, I. OH, T. LIM, *Int. J. Hydrogen Energy* **2008**, *33*, 2783.
[21] E. Dong, H. Zhao, R. Zhang, L. Chen, W.-Q. Tao, *Electrochim. Acta* **2024**, *477*, 143772.
[22] Q. Shen, S. Dong, S. Li, G. Yang, *Electrochim. Acta* **2023**, *454*, 142326.
[23] X. Huang, Y. He, Y. Sun, L. Sun, T. Wang, X. Zhang, *J. Power Sources* **2024**, *603*, 234488.
[24] J. Shin, M. Son, S.-I. Kim, S. A. Song, D. H. Lee, *J. Power Sources* **2023**, *582*, 233546.
[25] Z.-H. Xuan, W.-Z. Fang, G.-R. Zhao, W.-Q. Tao, *Appl. Energy* **2025**, *377*, 124756.
[26] R. Fan, G. Chang, Y. Xu, J. Xu, *Energy* **2024**, *290*, 130128.
[27] G.-R. Zhao, W.-Z. Fang, C.-Z. Hu, K.-B. An, Z.-H. Xuan, W.-Q. Tao, *Int. Commun. Heat Mass. Transf.* **2025**, *167*, 109232.
[28] A. Zucconi, J. Hack, T. A. M. Suter, M. Braglia, P. R. Shearing, D. J. L. Brett, A. J. E. Rettie, *J. Power Sources* **2023**, *584*, 233574.
[29] Z. Zhao, M. D. Hossain, C. Xu, Z. Lu, Y.-S. Liu, S.-H. Hsieh, I. Lee, W. Gao, J. Yang, B. V. Merinov, W. Xue, Z. Liu, J. Zhou, Z. Luo, X. Pan, F. Zaera, J. Guo, X. Duan, W. A. Goddard, Y. Huang, *Matter* **2020**, *3*, 1774.
[30] M. Srinivasarao, D. Bhattacharyya, R. Rengaswamy, S. Narasimhan, *Int. J. Hydrogen Energy* **2010**, *35*, 6356.
[31] M. Ayoub, T. Böhm, M. Bierling, S. Thiele, M. Brodt, *J. Electrochem. Soc. 171*, 94503.
[32] N. Rajalakshmi, K. Dhathathreyan, *Chem. Eng. J.* **2007**, *129*, 31.
[33] P. Schneider, A.-C. Scherzer, B. D. Storey, M. Klingele, N. Zamel, D. Gerteisen, *J. Electrochem. Soc.* **2023**, *170*, 104505.
[34] S. Zhou, J. Dale-Heaps, E. Tavkaya, W. Du, D. Wan, R. Wang, P. R. Shearing, D. J. L. Brett, E. Engebretsen, R. Jervis, *Appl. Energy* **2024**, *376*, 124276.
[35] S. Chung, D. Shin, M. Choun, J. Kim, S. Yang, M. Choi, J. W. Kim, J. Lee, *J. Power Sources* **2018**, *399*, 350.
[36] S. Jang, M. Kim, Y. S. Kang, Y. W. Choi, S. M. Kim, Y.-E. Sung, M. Choi, *ACS Appl. Mater. Interfaces* **2016**, *8*, 11459.
[37] S. R. Choi, D. Y. Kim, W. Y. An, S. Choi, K. Park, S.-D. Yim, J.-Y. Park, *Mater. Sci. Energy Technol.* **2022**, *5*, 66.
[38] Y. Garsany, R. W. Atkinson, M. B. Sassin, R. M. Hjelm, B. D. Gould, K. E. Swider-Lyons, *J. Electrochem. Soc.* **2018**, *165*, F381.
[39] Y. Wan, D. Qiu, P. Yi, L. Peng, X. Lai, *Appl. Energy* **2022**, *312*, 118723.
[40] Y. Xiao, W. Zheng, J. Wang, B. Li, P. Ming, C. Zhang, *Appl. Energy* **2025**, *389*, 125759.
[41] M. Prokop, M. Drakselova, K. Bouzek, *Curr. Opin. Electrochem.* **2020**, *20*, 20.
[42] S. Zhou, L. Xu, P. Trogadas, L. Rasha, W. Du, P. R. Shearing, M.-O. Coppens, D. J. L. Brett, R. Jervis, *J. Power Sources* **2023**, *575*, 233184.